CHALMERS
UNIVERSITY OF TECHNOLOGY

Exhaust waste heat recovery from a heavy-duty truck engine: Experiments and simulations

Energy 238 (2022) 121698

Contents lists available at ScienceDirect

Energy

journal homepage: www.elsevier.com/locate/energy

Exhaust waste heat recovery from a heavy-duty truck engine: Experiments and simulations

Jelmer Rijpkema [a, *], Olof Erlandsson [b], Sven B. Andersson [a], Karin Munch [a]

[a] Mechanics and Maritime Sciences, Chalmers University of Technology, Gothenburg, Sweden
[b] TitanX Engine Cooling AB, Sölvesborg, Sweden

ARTICLE INFO

Article history:
Received 4 March 2021
Received in revised form
22 July 2021
Accepted 4 August 2021
Available online 14 August 2021

Keywords:
Experiments
Exhaust gases
Heavy-duty
Internal combustion engine
Organic rankine cycle (ORC)
Reciprocating piston expander
Long haul truck
Waste heat recovery

ABSTRACT

Waste heat recovery using an (organic) Rankine cycle is an important and promising technology for improving engine efficiency and thereby reducing the CO_2 emissions due to heavy-duty transport. Experiments were performed using a Rankine cycle with water for waste heat recovery from the exhaust gases of a heavy-duty Diesel engine. The experimental results were used to calibrate and validate steady-state models of the main components in the cycle: the pump, pump bypass valve, evaporator, expander, and condenser. Simulations were performed to evaluate the cycle performance over a wide range of engine operating conditions using three working fluids: water, cyclopentane, and ethanol. Additionally, cycle simulations were performed for these working fluids over a typical long haul truck driving cycle. The predicted net power output with water as the working fluid varied between 0.5 and 5.7 kW, where the optimal expander speed was dependent on the engine operating point. The net power output for simulations with cyclopentane was between 1.8 and 9.6 kW and that for ethanol was between 1.0 and 7.8 kW. Over the driving cycle, the total recovered energy was 11.2, 8.2, and 5.2 MJ for cyclopentane, ethanol, and water, respectively. These values correspond to energy recoveries of 3.4, 2.5, and 1.6%, respectively, relative to the total energy requirement of the engine. The main contribution of this paper is the presentation of experimental data on a complete Rankine cycle-based WHR system coupled to a heavy-duty engine. These results were used to validate component models for simulations, allowing for a realistic estimation of the steady-state performance under a wide range of operating conditions for this type of system.

1. Introduction

The continuous increase of anthropogenic greenhouse gas (GHG) emissions is causing severe adverse effects on the climate. Consequently, the global energy system must rapidly reduce its emissions [1]. Because heavy-duty (HD) trucks and buses are responsible for over 5% of the total GHG emissions in Europe [2], ways to reduce emissions from HD vehicles are needed. As a result, the European Union has imposed CO_2 emission standards for HD vehicles that require emission reductions of 15% from 2025 onwards and 30% from 2030 onwards, relative to the 2019 baseline [3]. Several technologies and powertrain concepts have been proposed to help meet these requirements, including improvements in combustion and air management efficiency, predictive powertrain control, hybridization, reduction of friction and other losses, renewable fuels, hydrogen, fuel cells, and waste heat recovery (WHR) [4,5]. WHR systems generate power from the waste heat of the heat sources in a HD engine, namely the charge air cooler (CAC), the exhaust recirculation (EGR) cooler, the engine coolant, or the exhaust gases [6]. Many different WHR concepts and technologies exist, including turbocompounding [7], thermoacoustic convertors [8], thermoelectric generators [9], and technologies based on thermodynamic cycles such as the Brayton [10], Stirling [11], Rankine [12], or various flash cycles [6]. Systems based on the (organic) Rankine cycle (ORC) have been found to achieve good performance and flexibility, although the added weight, complexity, and payback time remain obstacles to their commercial implementation [13].

In an ORC-based WHR system, waste heat is used to evaporate a working fluid at elevated pressure. The high pressure, high temperature fluid is then expanded, converting the heat energy into power, after which the fluid is condensed before entering the

* Corresponding author.
E-mail address: jelmer.rijpkema@chalmers.se (J. Rijpkema).

https://doi.org/10.1016/j.energy.2021.121698

pump. The goal of the WHR system is to maximize the net power output, while maintaining superheated vapor conditions at the inlet of the expander [14]. The performance of such systems in heavy-duty Diesel (HDD) engines has been the topic of many publications (mostly simulation studies), with reported fuel savings of over 5% [13,15]. Important issues addressed in these studies include heat source selection [16], the choice of working fluid [16–18], heat exchanger modeling [19,20], expander selection and performance [21], cycle configuration [22], and techno-economic performance optimization [23]. Due to the transient operation of an internal combustion engine, much recent research has focused on developing and validating dynamic models and controls for ORC systems in HD engines [14,24–27]. In addition to the academic interest, ORC systems for HDD engines have attracted considerable interest from major automotive industry firms in the last decade, including AVL [28], BMW [29,30], Bosch [31], Cummins [32,33], Daimler [34], Honda [35], Mahle [36], Scania [37], Volkswagen [38], Volvo Car Corporation [39,40], and Volvo Group [24,41].

A number of notable recent publications concerning experimental research on WHR from HDD engines are briefly discussed below and listed in Table 1. Seher et al. [31] reported an experimental study on a Rankine cycle with water for a 12 L HDD engine. A maximum power output of 14 kW was obtained with a piston expander, corresponding to 4.3% of the engine power, while 9 kW (2.8%) was achieved with a turbine expander. Based on simulations it was concluded that water or ethanol with a piston or ethanol with a turbine were the preferred solutions, giving a maximum relative power of 5.3%. Furukawa et al. [42] tested two ORC systems for WHR from a downsized HDD engine. In their first system, heat was recovered from the engine coolant and EGR gases, reducing fuel consumption by 3.8%. In their second system, the coolant temperature was increased from 86 to 105 °C, the exhaust gas was included as a heat source, and a recuperator was added, improving the fuel consumption reduction to 7.5%. Yang et al. [43] used an ORC with R245fa and a screw expander to recover up to 28.6 kW (10.2%) from a HDD engine. Zhang et al. [44] also used a screw expander in an ORC with R123 for exhaust heat recovery from a HDD engine and achieved a maximum power of 10.4 kW. Bettoja et al. [41] performed experiments on two systems for two different engines: a Volvo US10 and a CRF Cursor 11. For the Volvo engine, heat was recovered from the exhaust and EGR with a water/ethanol mixture. An orifice was used instead of an expander and the system was predicted to achieve a relative power recovery between 1.5 and 3%. For the CRF engine, a system with R245fa and a turbine was used, giving a maximum power output of 2.5 kW. Latz et al. [45] used a similar setup as in this paper featuring the same engine, but recovered heat from the EGR cooler using a reciprocating piston expander and water. The maximum recovered power in this case was 2.7 kW. Simulations were performed to identify important parameters for performance improvement of the EGR evaporator and piston expander. Shu et al. [46] compared the working fluids R123 and R245fa in a WHR system with an intermediate oil loop connected to the exhaust of an HDD engine. No expander was installed in the system, but, by using estimated efficiencies, a maximum power output of 9.7 kW for R123 was predicted. In another study, Yu et al. [47] replaced the oil loop with another Rankine cycle with water. This improved the estimated power output to 12.7 kW or 5.6% in relative terms. More recently, Shi et al. [48] used the same engine for WHR from the exhaust and engine coolant with four configurations of a CO_2 transcritical Rankine cycle. Using estimated efficiencies, the maximum power output was predicted to be 3.5 kW. Guillaume et al. [49] simulated the exhaust conditions of a HDD engine using a boiler with thermal oil and concluded that R1233zd(E) performed better than R245fa in their experiments, providing a maximum power output of 2.8 kW with a turbine expander. Alshammari et al. [50] recovered the exhaust heat using an ORC with R1233zd(E), a turbine, and an intermediate thermal oil loop, giving a maximum recovered power of 6.3 kW. Their results were complemented by CFD simulations and evaluations of the radial inflow turbine performance. In a more recent study [51], the same group subsequently tested the same engine with a WHR system featuring a thermal loop, a turbine, and Novec649 as the working fluid. The maximum power output in this case was 9.1 kW (11.2%). Additionally, they showed that increasing the cooling water temperature and superheating temperature reduced the performance of the turbine.

Although there have been many publications regarding the use of ORC for WHR in HDD engines, there is still a lack of publicly available experimental data. This is partly because publications from industry often report performance improvements without providing much detail on the cycle components. Additionally, many publications reporting results of dynamic models often present experimental data that was used to validate the model. These results only specify the controlled parameters (e.g. mass flow rate or evaporator outlet temperature) without offering insight into the cycle or component performance. In this paper, an experimental

Table 1
Recent experimental studies on WHR from HDD engines using ORCs.

Reference	Year	Engine	Heat source	Fluids(s)	Expander	$\dot{W}_{max}$	$\frac{\dot{W}_{max}}{\dot{W}_{eng}}$
-	-	L/kW	-	-	-	kW	%
Seher et al. [31]	2012	12.0/326	Exhaust	Water	Piston, Turbine	14	4.3
Furukawa et al. [42]	2014	9.0/-	Exhaust, EGR, Coolant	HFE	Turbine	–	7.5
Yang et al. [43]	2014	9.7/280	Exhaust	R245fa	Screw	28.6	10.2
Zhang et al. [44]	2014	-/250	Exhaust	R123	Screw	10.4	4.2
Bettoja et al. [41]	2016	11.1/353	Exhaust	R245fa	Turbine	2.5	–
		12.7/317	Exhaust, EGR	Water/Ethanol	–	–	3.0
Latz et al. [45]	2016	12.8/373	EGR	Water	Piston	2.7	
Shu et al. [52]	2016	8.4/243	Exhaust	R123, R245fa	–	9.7	4.0
Yu et al. [47]	2016	8.4/243	Exhaust	Water, R123	–	12.7	5.6
Guillaume et al. [49]	2017	-/ -	Exhaust	R245fa, R1233zd(E)	Turbine	2.8	–
Shi et al. [48]	2017	8.4/243	Exhaust, Coolant	CO_2	–	3.5	–
Alshammari et al. [50]	2018	7.3/206	Exhaust	R1233zd(E)	Turbine	6.3	7.6
Alshammari et al. [51]	2019	7.3/206	Exhaust	Novec649	Turbine	9.1	11.2

setup consisting of a Rankine cycle with water connected to the exhaust of a HDD engine is evaluated and used to calibrate and validate models of the relevant cycle components. The components are then used to develop a realistic Rankine cycle model to determine the optimum performance in a driving cycle for a variety of working fluids. Simulation of the driving cycle allows for an evaluation of the performance of the WHR system over the full operational range of the engine. However, the corresponding transient effects are considered outside the scope of this paper, and are, therefore, not taken into account. The goal of this publication is to provide detailed experimental data on a full Rankine system connected to a HDD engine, and to develop models that give an accurate prediction of the WHR system performance under realistic operating conditions.

2. Experimental setup

The experimental setup is shown in Fig. 1 and a schematic overview is presented in Fig. 2. The setup consists of a heavy-duty truck engine whose exhaust gases are used as the heat input for a WHR system based on a Rankine cycle using water as the working fluid. Both the engine and WHR system are placed in an engine test cell in which the temperature and pressure can be regulated. Only steady-state measurements are available from the engine due to limitations on the engine brake. The setup is monitored and controlled from the adjacent control room using multiple modules installed in two National Instruments CompactRIO 9074 controllers coupled to a Labview interface. Several cameras and a connecting window allow for visual observations while running the setup. Sensor data was measured at a sampling frequency of 10 Hz which was written to disk every second. For each measuring point, three minutes of data were collected and averaged.

The engine is a turbocharged 12.8 L Volvo Diesel engine with charge air cooling (CAC) and exhaust gas recirculation (EGR); its specifications are shown in Table 2. A Schenck D900-1e water brake is used to control the engine speed. The engine torque is controlled by regulating the fuel flow through manual operation of the gas pedal. Fuel is provided from a Diesel tank located in a separate fuel storage.

Fig. 2 shows the main components of the WHR system; their specifications are listed in Table 3 together with the corresponding controller where applicable. The WHR system is a typical Rankine cycle with water as the working fluid. The suction side of the pump is connected to the buffer tank, which is open to the atmosphere. A controllable pump bypass valve (BPV) is installed because the flow

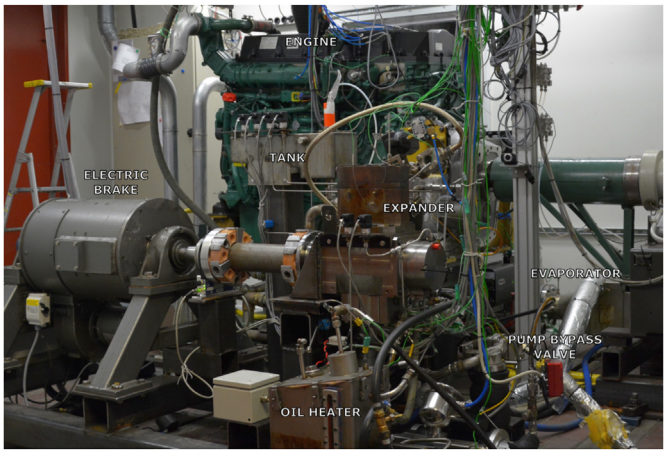

Fig. 1. Experimental setup.

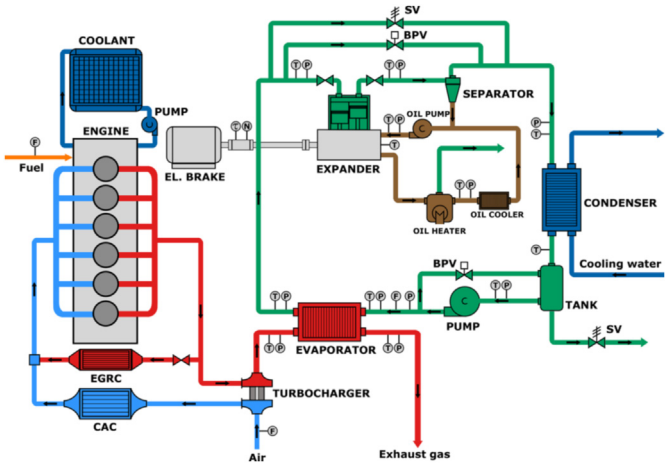

Fig. 2. Schematic depiction of the experimental setup.

Table 2
Engine specifications.

Type	Volvo D13 US 2010
Configuration	4 Stroke/6 Cylinder inline/EGR
Peak power	373 kW (500 hp)
Peak torque	2373 Nm
Compression ratio	16.0:1
Bore x Stroke	131 × 158 mm
Displacement	12.8 L
Aspiration	Turbocharged

at the minimum pump speed would otherwise be too large to permit full evaporation under low load engine operating conditions. The evaporator uses the exhaust gases downstream the engine turbocharger to evaporate and superheat the water from the pump. It is specifically manufactured for this experimental setup by TitanX and is shown in Fig. 3. Under start-up and shut-down conditions, the fluid leaving the evaporator is not always fully evaporated. Therefore, the expander inlet and outlet valves are closed and the controllable expander bypass valve (BPV) open so the flow bypasses the expander, preventing liquid from entering. The expander is a reciprocating piston type with two cylinders using a separate crankcase with its own oil circuit. Water enters the expander as superheated steam and exits as a two-phase mixture at low pressure. During expansion, the expander converts some of the energy in the steam into power via an electric motor, which controls the expander speed. Since some of the steam enters the crankcase of the expander, the oil is heated to 140 °C, causing this water to evaporate and be expelled to the environment. To prevent hot oil from entering the oil pump, the oil is subsequently cooled. In the cycle, the oil is separated from the water and the low-pressure two-phase mixture enters the condenser, where it is condensed and subcooled to around 15 °C using process water from the test cell. From the condenser, the subcooled water enters the buffer tank. To avoid overpressures in the system, safety valves (SV) are installed on the high and low pressure sides of the cycle.

Fig. 2 also shows the locations of the different sensors in the system; the details and accuracies are shown in Table 4. The engine speed and torque were taken from the Schenck D900-1e measurements and the fuel flow using an AVL 730 fuel balance. The engine inlet air flow was measured using the pressure drop over a calibrated venturi tube, sufficiently upstream the turbocharger to avoid flow pulsations. Pressures in the system were measured using WIKA A-10 pressure transmitters with different ranges depending

Table 3
Specifications of cycle components.

Component	Brand	Type	Controller
Condenser	Modine	Plate, counter-current flow	
Evaporator	TitanX	Plate, cross-counter flow	
Expander	Voith	Reciprocating piston, 2-cylinder	
Expander bypass valve	Swagelok SS-18RS8	Integral-bonnet needle	Hanbay MCL-000 AF
Expander electric motor	David McClure LTD	400 V, 3-phase, 37 kW	Parker DC590+ Integrator 2
Pump	Danfoss PAH2	Axial piston	
Pump bypass valve	Swagelok SS-1RS4	Integral-bonnet needle	Hanbay MCL-000 AF
Pump electric motor	Hoyer HMA2 90L-4	230 V, 3-phase, 1.5 kW	IMO iDrive EDX-220-21-E

Fig. 3. Exhaust evaporator.

Table 4
Measurement devices accuracy.

Input	Type	Range	Accuracy	Unit
Engine speed	Schenck D900-1e	0–6500	±2	rpm
Engine torque	Schenck D900-1e	−4000–4000	±8	Nm
Expander speed	HBM T40B	0–20,000	±10	rpm
Expander torque	HBM T40B	−500–500	±0.25	Nm
Fuel flow	AVL 730	0–150	±0.9	kg/h
Mass flow	Micro Motion F025S	0–100	±0.2	g/s
Cycle high pressure	WIKA A-10	0–60	±0.6	bar(g)
Cycle low pressure	WIKA A-10	0–6	±0.06	bar(g)
Exhaust pressure	WIKA A-10	0–2.5	±0.03	bar(g)
Pressure drop	Yokogawa EJA110E	0–5000	±2.75	Pa
Temperature	RS Pro Type K	−75–1100	±1.5	°C

on the location. Temperature measurements were taken with 3 mm diameter RS Pro Type K thermocouples. In the Rankine cycle, the mass flow was measured with a coriolis mass flow meter and the expander speed and torque were both measured with an universal digital torque transducer.

3. Experimental results and component calibration

In this section the experimental results and modeling relations of the main components in the WHR system are combined in separate sections: *Engine*, *Pump*, *Pump Bypass Valve*, *Evaporator*, *Expander*, and *Condenser*. If the results are used to calibrate and/or validate the component, it is also shown. The last section shows the comparison of the experiments and simulations for the full cycle performance. A total of six different experimental sets were used, as listed and described in Table 5, which shows the corresponding number of experimental points and a description for each experimental set.

Multiple quantities derived from the performed measurements are presented in the subsequent sections. The standard deviations for the measured (i.e. non-derived) data are represented by error bars in the figures. Table 6 shows the maximum measurement error based on the standard rules for error propagation [53].

3.1. Engine

The experimental measurements of the exhaust mass flow and outlet temperature are shown in Figs. 4 and 5. These results are averages based on the measurements acquired in experimental set 5 (see Table 5). The engine operating points are named in accordance with the conventions of the European Stationary Cycle (ESC): the letters A, B, and C indicate different engine speeds, and the numbers 25, 50, 75, and 100 indicate the load percentages at the corresponding speed [54]. An additional highway (HW) point was tested, which represents typical engine conditions during highway driving. These measurements were used to define the heat input conditions used in the cycle model. The original measured mass flows were somewhat higher than those obtained in previous experimental studies on similar engines, suggesting that the mass flow values measured in the test cell were systematically biased upward. Consequently, the original mass flow values were multiplied by an error factor of 0.75 to obtain more realistic values. The mass flows presented in Fig. 4 have been corrected in this manner.

3.2. Pump

The mass flow from the pump is determined from its inlet density (ρ_{in}) and volume flow ($\dot{V}_{pmp}$) using Eq. (1). The specifications of the pump are shown in Table 7.

$$\dot{m}_{pmp} = \rho_{in}\dot{V}_{pmp} \tag{1}$$

Although the axial piston pump is relatively insensitive to pressure changes, the actual volume flow ($\dot{V}_{pmp}$) is calculated by applying a correction to the theoretical flow ($\dot{V}_{th}$):

$$\dot{V}_{pmp} = \dot{V}_{th} - \dot{V}_{corr}\frac{p_{pmp,\,out}}{p_{max}} \tag{2}$$

The theoretical flow in L/min is defined as:

$$\dot{V}_{th} = V_{pmp}N_{pmp} \tag{3}$$

The flow correction in L/min depends on the pump outlet pressure ($p_{pmp,\,out}$) in bar and the pump speed (N_{pmp}) in rpm. This is

Table 5
Numbering, quantity of experimental points (Qty.) and description of the experimental sets.

Set	Qty.	Description
1.	7	Cold system, no expander, low pressure, pump validation
2.	6	Cold system, no expander, high pressure, pump validation
3.	13	Cold system, no expander, pump bypass valve calibration
4.	16	Cold system, no expander, pump bypass valve validation
5.	28	Hot system, no expander, engine results, evaporator calibration, condenser results
6.	41	Hot system, expander calibration, cycle validation

Table 6
Measurement error for the derived quantities.

Quantity	Symbol	Max. Error
Engine mass flow	$\dot{m}_{eng}$	±5.9%
Pump power	$\dot{W}_{pmp}$	±9.4%
Bypass valve effective area	A_{bpv}	±4.5%
Evaporator heat transfer rate	$\dot{Q}_{evap}$	±6.8%
Expander filling factor	$\varphi_{f,\,is}$	±6.0%
Expander efficiency	η_{exp}	±8.9%
Expander power	$\dot{W}_{exp}$	±8.2%
Condenser heat transfer rate	$\dot{Q}_{cond}$	±7.9%

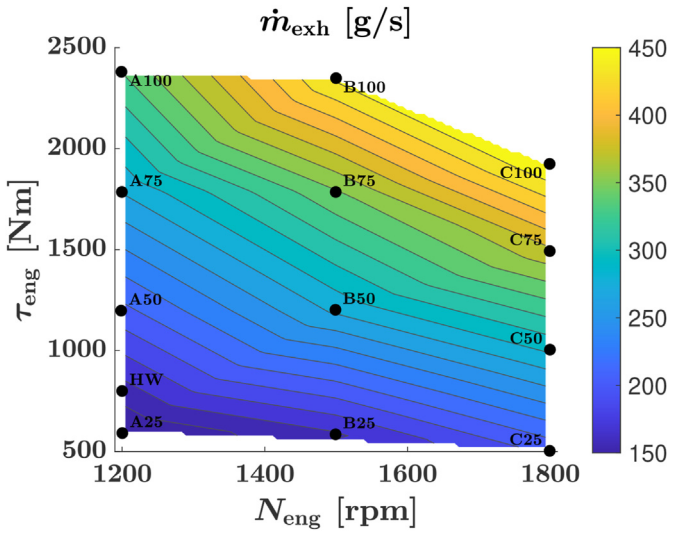

Fig. 4. Engine speed-torque map showing the measured engine exhaust mass flow. The measurements were corrected by a factor 0.75 based on an estimated error of the measured values.

approximated in Eq. (4) using technical data from the manufacturer [55].

$$\dot{V}_{corr} = -0.0001 N_{pmp} + 1.2 \tag{4}$$

The pump power can be calculated with an estimated efficiency:

$$\dot{W}_{pmp} = \dot{m}_{pmp}(h_{pmp,\,out} - h_{pmp,\,in}) \Big/ \eta_{pmp} \tag{5}$$

To validate the pump model, measurements were conducted at a low (set 1) and a high (set 2) pressure. In both cases, no heat was added to the system, the pump bypass valve was fully closed, the expander was not running, and the expander bypass valve was used to control the pressure. The results of the experiments and simulations are shown in Fig. 6, indicating that a good agreement was achieved.

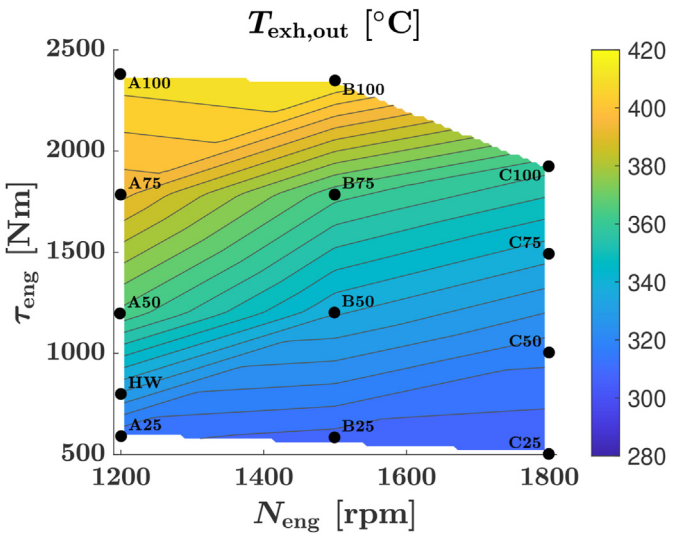

Fig. 5. Engine speed-torque map showing the measured engine exhaust outlet temperature.

Table 7
Pump specifications [55].

Maximum pressure	p_{max}	100	bar
Displacement volume	V_{pmp}	0.002	L

3.3. Pump bypass valve

The pump bypass valve is modeled as an incompressible flow valve, as shown in Eq. (7). The discharge coefficient (C_d) and valve area (A) can be combined into an effective area (A_{bpv}).

$$\dot{m}_{bpv} = C_d A \sqrt{2\rho_{in}(p_{in} - p_{out})} = A_{bpv}\sqrt{2\rho_{in}(p_{in} - p_{out})} \tag{6}$$

Although the pump bypass mass flow ($\dot{m}_{bpv}$) is not known, the evaporator mass flow ($\dot{m}_{evap}$) was measured and can be subtracted from the pump mass flow ($\dot{m}_{pmp}$), available from the pump model:

$$\dot{m}_{bpv} = \dot{m}_{pmp} - \dot{m}_{evap} \tag{7}$$

The effective area is a function of the valve position (x_{bpv}) and is calibrated using the data from experimental set 3. The calibrated model consists of a combination of two linear functions of which the coefficients are shown in Table 8.

The resulting effective area as a function of the valve position is shown on the left on Fig. 7, together with the corresponding experimental data. During these experiments no heat was added to the system, the pump bypass valve position was controlled, the expander was not running, and the expander bypass valve was held at a fixed position. The corresponding results for the mass flow is shown on the right of Fig. 7, along with results obtained under

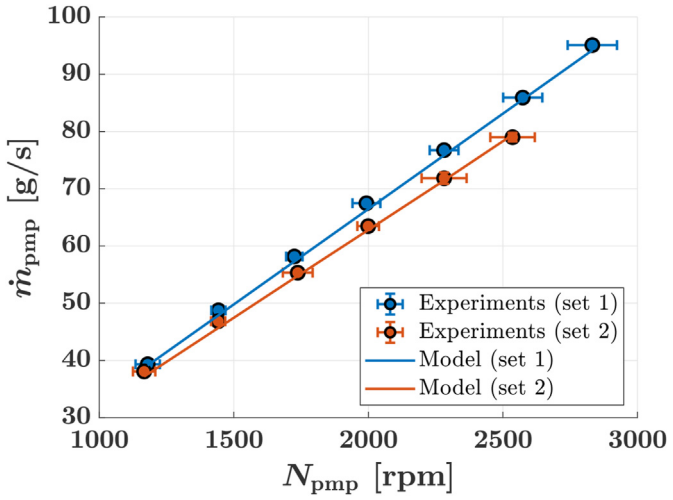

Fig. 6. The mass flow as a function of the pump speed and pump outlet pressure.

Table 8
Pump bypass valve coefficients.

x_{bpv}	%	0	1	2	7	100
A_{bpv}	mm^2	0	0.25	0.35	1	2.65

different conditions (set 4) that were used for model validation. Good agreement with the experiments is observed for both for the calibration and validation data sets.

3.4. Evaporator

The exhaust evaporator is a cross-counter flow plate heat exchanger with fins; its heat transfer area is depicted schematically in Fig. 8. The exhaust flow side has one pass and 36 channels, while the water side has three passes and 35 channels. The dimensions of the heat exchanger are listed in Tables 9 and 10. The model only accounts for heat transfer; the pressure drop over the evaporator is ignored.

Heat transfer is modeled using fin-specific equations. The geometric parameters of the fins are computed using the values presented in Table 10 and the following equations [56]:

$$D_{\mathrm{h}} = \frac{4 s_{\mathrm{f}} b L_{\mathrm{f}}}{2(s_{\mathrm{f}} L_{\mathrm{f}} + b L_{\mathrm{f}} + t_{\mathrm{f}} b) + t_{\mathrm{f}} s_{\mathrm{f}}} \tag{8}$$

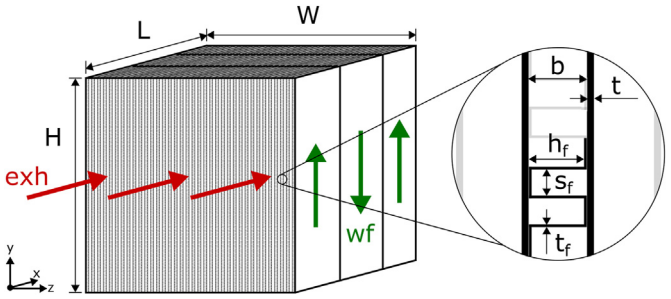

Fig. 8. Schematic depiction of the heat transfer area of the exhaust evaporator.

Table 9
Heat exchanger dimensions.

Heat exchanger length	L	144	mm
Heat exchanger width	W	241	mm
Heat exchanger height	H	247	mm
Channel height	b	3.00	mm
Plate thickness	t	0.40	mm
Fluid-specific		**wf**	**exh**	
Number of channels	n_{ch}	35	36	–
Number of passes	n_{pass}	3	1	–
Number of fins in x-dir.	$n_{\mathrm{f,\,x}}$	96.0	45.4	–
Number of fins in y-dir.	$n_{\mathrm{f,\,y}}$	77.8	164.7	–
Number of fins	n_{f}	7468	7468	–
Total flow area	A_{c}	4309	22,808	mm^2

$$A_{\mathrm{flow}} = s_{\mathrm{f}} h_{\mathrm{f}} \tag{9}$$

$$A_{\mathrm{base}} = 2(s_{\mathrm{f}} L_{\mathrm{f}} + t_{\mathrm{f}}(s_{\mathrm{f}} - t_{\mathrm{f}})\,/\,2) \tag{10}$$

$$A_{\mathrm{fin}} = 2(h_{\mathrm{f}} L_{\mathrm{f}} + h_{\mathrm{f}} t_{\mathrm{f}}) \tag{11}$$

For each pass and channel the number of fins for the working fluid and exhaust can be calculated:

$$n_{\mathrm{f,\,x,\,wf}} = \frac{L}{p_{\mathrm{f}}},\quad n_{\mathrm{f,\,y,\,wf}} = \frac{H}{L_{\mathrm{f}}} \tag{12}$$

$$n_{\mathrm{f,\,x,\,exh}} = \frac{L}{L_{\mathrm{f}}},\quad n_{\mathrm{f,\,y,\,exh}} = \frac{H}{p_{\mathrm{f}}} \tag{13}$$

As a result, the total cross-sectional area (or total flow area) for the flow can be calculated:

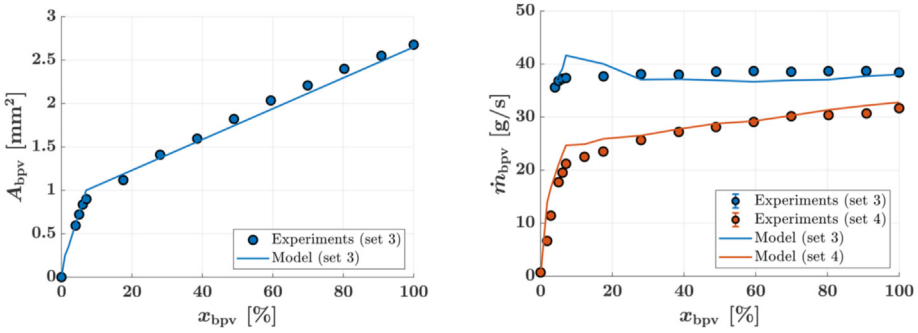

Fig. 7. Pump bypass valve effective area (left) and mass flow (right) as a function of the bypass valve position.

Table 10
Fin geometry.

Spacing	s_f	1.35	mm
Thickness	t_f	0.15	mm
Strip flow length	L_f	3.175	mm
Pitch	p_f	1.50	mm
Effective channel height	h_f	2.85	mm
Hydraulic diameter	D_h	1.791	mm
Flow area	A_{flow}	3.848	mm^2
Base area	A_{base}	8.753	mm^2
Fin area	A_{fin}	18.95	mm^2

$$A_{c,\,wf} = n_{ch,\,wf}\frac{n_{f,\,x,\,wf}}{n_{pass,\,wf}}A_{flow} \tag{14}$$

$$A_{c,\,exh} = n_{ch,\,exh}\frac{n_{f,\,y,\,exh}}{n_{pass,\,exh}}A_{flow} \tag{15}$$

The mass flux (G) for the exhaust and water sides is calculated by dividing the mass flow by the corresponding cross-sectional area ($G = \dot{m}/A_c$). With these definitions and the associated thermodynamic and transport properties, the Reynolds number (Re), the Prandtl number (Pr), and the heat transfer coefficient (α) can be determined using the Nusselt (Nu) number. For single-phase heat transfer, the following expression for the Nusselt number [56] is used:

$$\mathrm{Nu} = j\mathrm{RePr}^{1/3} \tag{16}$$

Where:

$$j = 0.652\mathrm{Re}^{-0.540}\left(\frac{s_f}{h_f}\right)^{-0.154}\left(\frac{t_f}{L_f}\right)^{0.150}\left(\frac{t_f}{s_f}\right)^{-0.068} \cdot\left[1 + 5.269\cdot10^{-5}\mathrm{Re}^{1.34}\left(\frac{s_f}{h_f}\right)^{0.504}\left(\frac{t_f}{L_f}\right)^{0.456}\left(\frac{t_f}{s_f}\right)^{-1.06}\right]^{0.1} \tag{17}$$

The two-phase heat transfer coefficient is the sum of the nucleate boiling (α_{nb}) and convective (α_{cv}) components [56]:

$$\alpha = \alpha_{nb} + \alpha_{cv} \tag{18}$$

The nucleate boiling component is a function of the heat flux ($\dot{q}$) for each element, the molecular weight (M_w), and the reduced pressure (p_{crit}), and is defined as:

$$\alpha_{nb} = 55\dot{q}^{2/3}M_w^{-1/2}\left(\frac{p}{p_{crit}}\right)^{0.225}\left[-\log_{10}\left(\frac{p}{p_{crit}}\right)\right]^{-0.55} \tag{19}$$

The convective component is obtained from the saturated liquid heat transfer coefficient (α_l), which is computed using Eq. (16) with saturated liquid properties. This coefficient is then multiplied by a factor (F) that depends on the steam quality (x) and the saturated liquid and vapor densities (ρ_l, ρ_v) and viscosities (μ_l, μ_v):

$$\alpha_{cv} = F\alpha_l \tag{20}$$

$$F = \left(1 + \frac{28}{X_{tt}}\right)^{0.372} \tag{21}$$

$$X_{tt} = \left(\frac{1-x}{x}\right)^{0.9}\left(\frac{\rho_v}{\rho_l}\right)^{0.5}\left(\frac{\mu_v}{\mu_l}\right)^{0.1} \tag{22}$$

To solve the heat transfer equations, the heat exchanger is discretized into a set of elements as shown in Fig. 9. A low resolution model is compared to a high resolution TitanX model whose settings are shown in Table 11. The heat transfer surface (A_s) is the combined base (A_{base}) and fin (A_{fin}) surface:

$$A_{s,\,el} = A_{base,\,el} + A_{fin,\,el} \tag{23}$$

The heat transfer is calculated for all channels based on the total surface area for each element:

$$A_{s,\,el,\,tot} = n_{ch,\,wf}A_{s,\,el} \tag{24}$$

For each element the heat transfer can be calculated:

$$\dot{Q}_{el} = U_{el}A_{s,\,el,\,tot}(T_{exh,\,el} - T_{wf,\,el}) \tag{25}$$

The overall heat transfer coefficient (U) consists of the sum of the separate contributions:

$$\frac{1}{U} = \frac{1}{\alpha_{wf}} + \frac{t_w}{\lambda_w} + \frac{1}{\alpha_{exh}} \approx \frac{1}{\alpha_{wf}} + \frac{1}{\alpha_{exh}} \tag{26}$$

The experimental and simulation results of the evaporator heat transfer rate and outlet temperature are shown in Fig. 10, based on experimental set 5 from Table 5. Experiments were performed at every engine operating point shown in Figs. 4 and 5 (A25-C100). In these experiments, the pump and pump bypass valve position were controlled to maintain a constant mass flow at each operating point. The expander was not running and the expander bypass valve was used to control the pressure. Both the low resolution model and the TitanX model exhibit good agreement with the experiments. However, it should be noted that in most cases the available heat from the exhaust gases was so large that the water was superheated to a temperature close to the exhaust gas inlet temperature. Increasing the mass flow would reduce the evaporator outlet temperature of the water, but the magnitude was difficult to control experimentally. Because of the relatively small mass flows and high latent heat of water, small deviations in mass flow caused large deviations in the evaporator outlet temperature. Another possible source of error is that the temperatures were measured at a single location, slightly downstream of the evaporator outlet. This could cause variations between the experimental values due to heat loss and local effects, leading to deviations from the model values. However, since the heat transfer to the working fluid is the most important for the prediction of the cycle performance, the model can still be used in the cycle simulations.

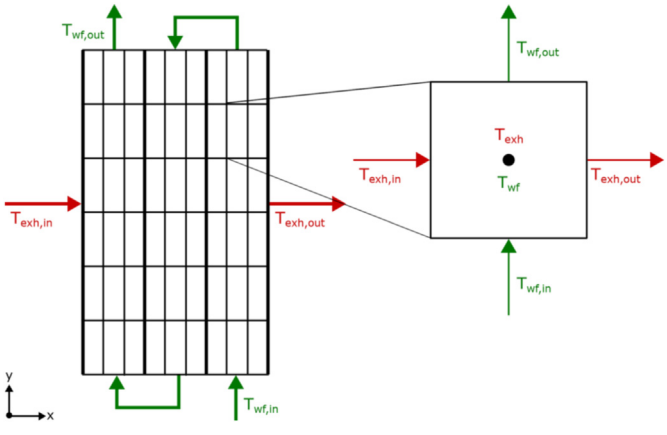

Fig. 9. Discretization of the exhaust evaporator.

Table 11
Heat exchanger geometry for each element.

		Model	TitanX	
Number of els. in x-dir.	$n_{el,\,x}$	6	9	–
Number of els. in y-dir.	$n_{el,\,y}$	3	10	–
Number of fins	$n_{f,\,el}$	415	83	–
Base area	$A_{base,\,el}$	3631	726	mm^2
Fin area	$A_{fin,\,el}$	7864	1573	mm^2
Heat transfer area	$A_{s,\,el}$	11,495	2299	mm^2

3.5. Expander

The expander is an uniflow reciprocating piston expander with two cylinders of which the relevant geometrical specifications are shown in Table 12.

The expander model is based on a semi-empirical model for volumetric expanders [57] which is schematically shown in Fig. 11. The semi-empirical model consists of thermodynamic equations with tuning parameters that are determined by calibrating them against experimental results. Using these parameters, the deviations from ideal expander performance caused by pressure drops, leakage, heat losses, and mechanical losses can be determined. More details on the modeling, results, and validation of the expander were presented in a previous publication [58].

The operation of the expander is characterized by three main performance factors: the isentropic filling factor ($\varphi_{f,\,is}$), the expander efficiency (η_{exp}), and the isentropic effectiveness (ε_{is}). All three factors depend on the process conditions and expander operation. The isentropic filling factor ($\varphi_{f,\,is}$) is used to predict how much the expander mass flow will deviate from ideal conditions under isentropic outlet conditions. For a piston expander, the theoretical flow is equal to product of the expander speed (N_{exp}) and the difference between the available mass at inlet valve closing ($\rho_{exp,\,in} f_a V_{exp}$) and the trapped mass at exhaust valve closing ($\rho_{exp,\,out} f_p V_{exp}$). In all tested conditions, the expansion ended in the two-phase region. Therefore, the outlet conditions are based on the isentropic conditions ($\rho_{exp,\,out,\,is} f_p V_{exp}$). This leads to the following expression:

$$\dot{m}_{exp} = \left(\rho_{exp,\,in} f_a - \rho_{exp,\,out,\,is} f_p\right) \varphi_{f,\,is} V_{exp} \frac{N_{exp}}{60} \tag{27}$$

To predict the shaft power output of the expander ($\dot{W}_{exp}$), the expander efficiency is used:

$$\dot{W}_{exp} = \eta_{exp} \dot{m}_{exp} (h_{exp,\,in} - h_{exp,\,out,\,is}) \tag{28}$$

For the expander considered in this paper, not only the shaft power output, but also the leakage and heat loss effects were significant. Therefore, the isentropic effectiveness (ε_{is}) is introduced,

Table 12
Expander specifications.

Supply cut-off	f_a	0.16	–
Exhaust cut-off	f_p	0.78	–
Displaced volume	V_{exp}	0.8	L

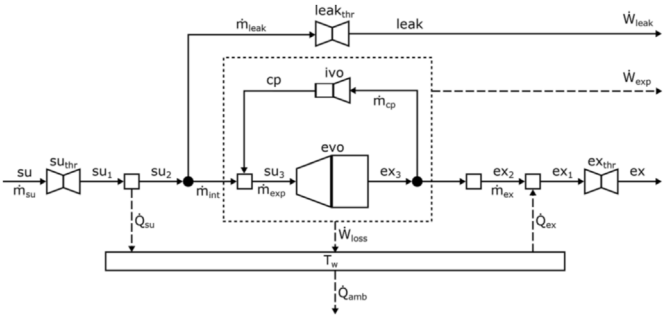

Fig. 11. Schematic depiction of the semi-empirical model used for the expander [58].

which is used to calculate the expander outlet enthalpy:

$$h_{exp,\,out} = h_{exp,\,in} - \varepsilon_{is}(h_{exp,\,in} - h_{exp,\,out,\,is}) \tag{29}$$

The resulting model outputs and the corresponding experimental values are shown on the left of Figs. 12 and 13, taken from experimental set 6. Experiments were performed at four engine operating points (A25, HW, A50, and B25). In the experiments, the pump and pump bypass valve position were controlled to provide a constant mass flow at each engine operating point, the expander speed was varied, and the expander bypass valve was closed. The results show that the expander mass flow is well captured by the isentropic filling factor. However, the shaft power is overpredicted for low pressure ratios (and corresponding low power outputs) and underpredicted at higher pressure ratios (and corresponding high power outputs). Since the expander efficiency is not only dependent on the pressure ratio, variations between experimental values for similar pressure ratios occur. Other important physical quantities include the expander speed, the cycle mass flow, and the expander inlet temperature. Deviations between model and experimental values are mainly attributed to the expansion in the two-phase region, high leakage rate in the expander, and the change in lubrication properties over time. These topics are discussed in more detail in a separate publication [58].

3.6. Condenser

The condenser is modeled as a heat sink only because neither detailed information on its geometry nor flow measurements on

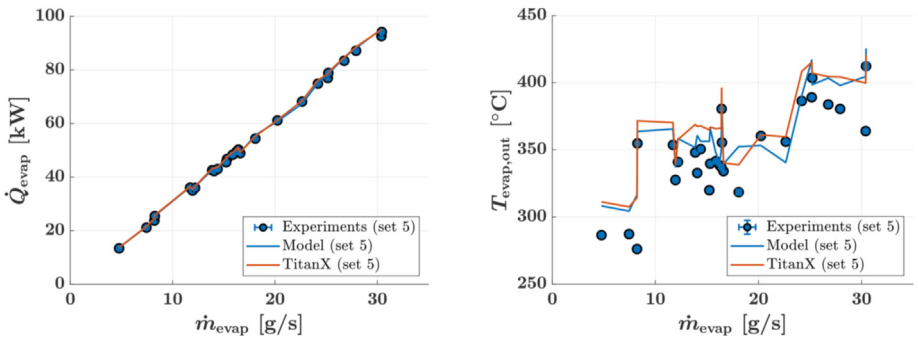

Fig. 10. Evaporator heat transfer rate (left) and outlet temperature (right) as a function of the mass flow.

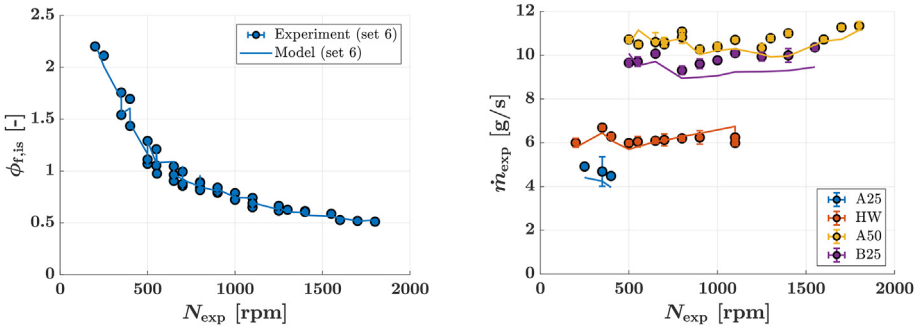

Fig. 12. The isentropic filling factor (left) and mass flow (right) of the expander as functions of the expander speed. Symbols indicate experimental results and lines indicate model outputs.

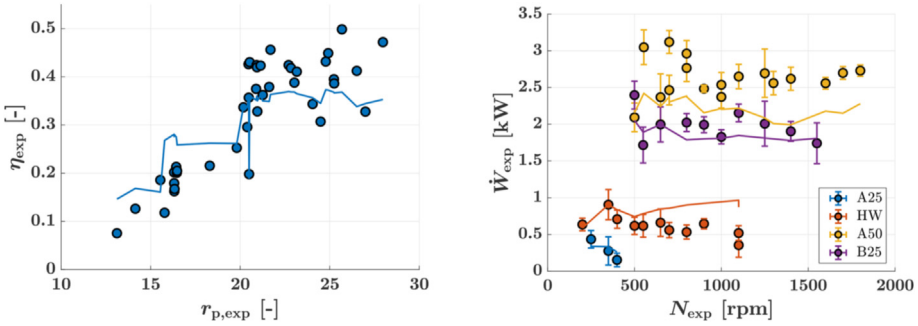

Fig. 13. The efficiency (left) and shaft power (right) of the expander as functions of the expander speed. Symbols indicate experimental results and lines indicate model outputs.

the process water used for cooling were available. Assuming no leakage of the working fluid, the modeled condenser flow was considered to be equal to the evaporator flow. This gives the following relations for the condenser:

$$\dot{m}_{cond} = \dot{m}_{evap} \tag{30}$$

$$\dot{Q}_{cond} = \dot{m}_{cond}(h_{cond,\,out} - h_{cond,\,in}) \tag{31}$$

Fig. 14 shows the experimental results of the condenser heat transfer rate from experimental set 5 in Table 5 together with the corresponding outlet temperatures. Experiments were performed at all of the engine operating points shown in Figs. 4 and 5 (A25-C100). In these experiments, the pump and pump bypass valve position were controlled to provide a constant mass flow at each engine operating point. The expander was not running and the expander bypass valve was used to control the pressure.

3.7. Rankine cycle

Simulations using the full cycle model incorporating all of the calibrated component models discussed in the preceding sections were performed in MATLAB [59] using fluid maps generated from the CoolProP [60] database. Fig. 15 shows the comparison of these simulation results to data from experiment set 6 in Table 5. Experiments were performed at four engine operating points (A25, HW, A50, and B25). The pump speed and pump bypass valve position were controlled to provide a constant mass flow, the expander speed was varied, and the expander bypass valve was closed.

The comparison of the model output to the experimental values shows that the pump outlet pressure is well captured. Deviations in the mass flow are mostly due to the sensitivity of the pump bypass valve model; small pressure changes cause large changes in the predicted flow through the bypass valve, leading to poor agreement between the model and experiment. Because the evaporator heat

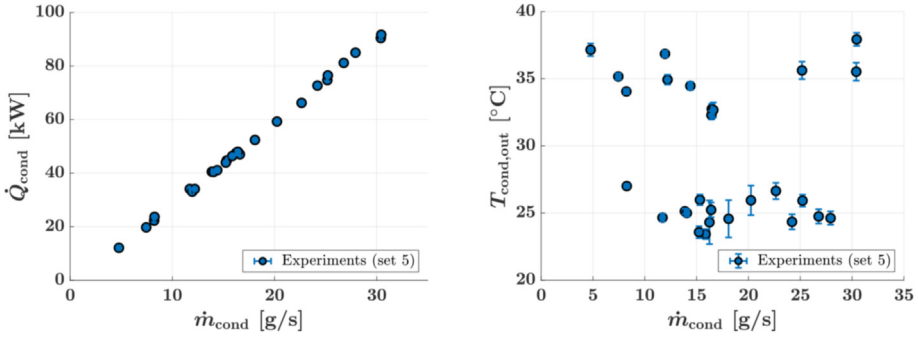

Fig. 14. Condenser heat transfer rate (left) and outlet temperature (right) as functions of the mass flow.

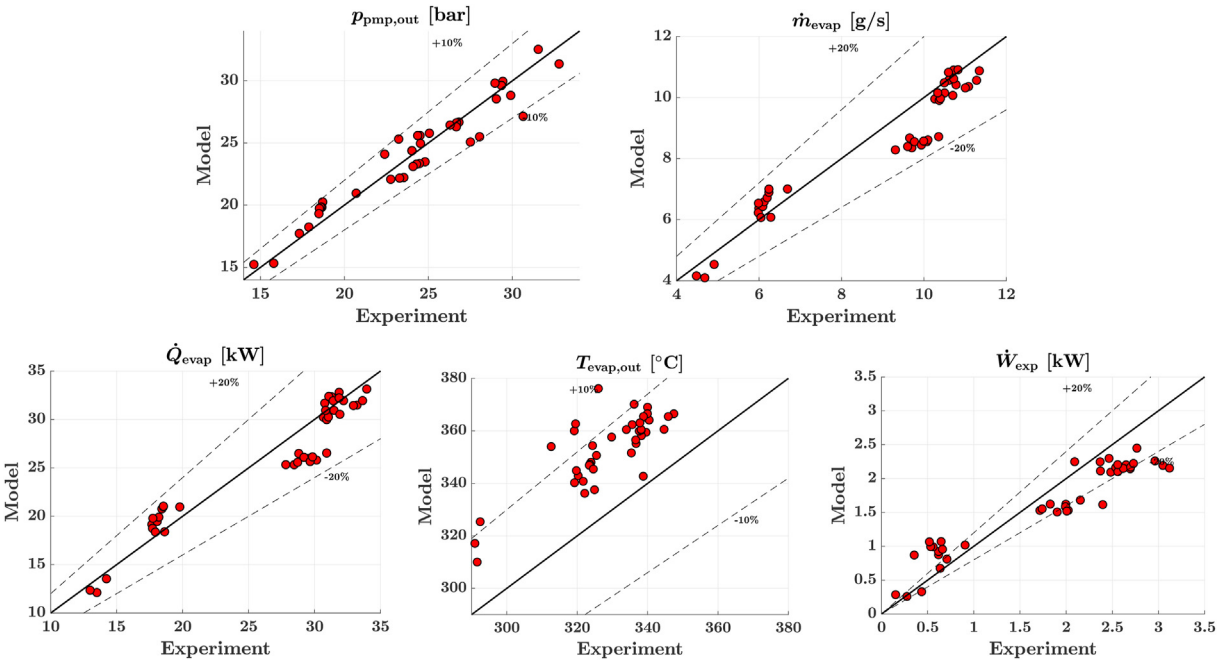

Fig. 15. Comparison of full cycle model outputs and experimental results.

transfer rate is proportional to the mass flow, the same effect is visible there. Also visible is the overprediction of the evaporator outlet temperature. Since no heat loss was considered in the models, the evaporator outlet temperatures of the working fluid almost reached the exhaust gas temperature. In reality, heat losses would lead to slightly lower temperature, explaining the deviations between simulations and experiments. Finally, the expander output power is significantly overpredicted at low power outputs and underpredicted at higher power outputs; the reasons for this are discussed in more detail in a separate publication [58].

The main source of error between the experimental and simulated values of the mass flow is the bypass valve model. A smaller pump in the experimental setup would possibly eliminate the need for a bypass valve. Alternatively, a more sophisticated model or calibration method for the bypass valve could improve the fit between experiments and simulations. Using a different working fluid could also help improve the fit. A fluid with a smaller latent heat would mean higher mass flows to extract the available heat. Simultaneously, the calibration and validation for the heat exchanger and the expander models could be improved. Another improvement would be the addition of pressure drop and heat loss correlations to the models. Although the figures show that the deviations between simulation and experimental results can be significant, the simulation results are based on physical models and the general trend is well-captured. This means that these models are a valid tool to compare the performance of different working fluids for operational range of the engine, which is done in the subsequent sections.

4. Simulation setup

The validated cycle model allows for predicting the performance of the WHR system under conditions outside the experimentally tested range (e.g. over a driving cycle) and with different working fluids. For this purpose, the bypass valve is removed from the original model, giving the cycle schematically depicted in Fig. 13. To obtain the desired mass flow, the pump is allowed to operate at speeds outside the range specified by the manufacturer.

4.1. Working fluids

To evaluate the performance of the WHR system, simulations were performed with two additional working fluids: cyclopentane and ethanol. These fluids were selected based on their promising thermodynamic performance in heavy-duty engine applications [17,61]. Previous studies by the authors [6,16,62], where different heat sources from the engine were evaluated for many different working fluids, also showed good thermodynamic performance for these two fluids. Additionally, they are environmentally friendly, relatively non-toxic, and non-corrosive, although flammability is a concern for both of them. Table 13 lists a number of important properties for the three working fluids.

4.2. Driving cycle

The model was calibrated against experimental data obtained in an engine test cell. However, temperatures under driving conditions are usually lower due thermal inertia and heat loss in the aftertreatment systems and exhaust piping. Therefore, the input conditions for the simulations were taken from a representative driving cycle for a 40 tonne EU6 Scania long haul truck driving on a European road. The vehicle speeds and road gradients for this driving cycle are shown in Fig. 16.

The exhaust outlet conditions (temperature and mass flow) during the driving cycle are divided into a four-by-four grid, as

Table 13
Properties of the selected working fluid.

Fluid	MW	p_{crit}	T_{crit}	GWP	ODP	Type
-	kg/kmol	bar	°C	-		
Cyclopentane	70.1	45.7	239	0	0	isentropic
Ethanol	46.1	62.7	240	0	0	wet
Water	18.0	220	374	0	0	wet

shown in Fig. 18. The percentages in the grid represent the relative duration of these conditions during the driving cycle. The green values indicate the duration for a positive torque on the engine and the red values indicate negative torque. The center points for all 16 elements were used as inputs for the steady-state simulations. Transient effects during the driving cycle were not taken into account.

4.3. Cycle performance

To run the simulations, a number of inputs and constraints were specified, as summarized in Table 14. The exhaust mass flow, temperature, and pressure were taken from the 16 previously defined operating conditions. Depending on whether the engine torque was positive or negative, the expander was coupled directly to the engine via a mechanical coupling or to an electrical generator. A subcooling temperature difference of 5 K was set to prevent vapor entering the pump. The pump mechanical efficiency, electrical generator efficiency, and the efficiency of the mechanical coupling between expander and engine were taken to be 0.50, 0.85, and 0.98, respectively. Only subcritical conditions were taken into account. The evaporator outlet temperature was limited to avoid thermal instability of the working fluid and overheating of suspended oil. To allow for temperature control, a minimum and maximum superheating temperature difference were set. The range of expander speeds was based on the specifications from the manufacturer [63]. The pump speed was not limited by these specifications; instead it was set to give the highest possible mass flow. No pressure drops in the components were considered and component heat losses other than the expander heat loss were ignored. A golden section search was performed to find the expander speed providing the maximum power output for the stated inputs and constraints.

Cycle performance is evaluated based on the net (shaft) power and thermodynamic efficiency:

$$\dot{W}_{\text{net}} = \dot{W}_{\text{exp}} - \dot{W}_{\text{pmp}} \tag{32}$$

$$\eta_{\text{th}} = \frac{\dot{W}_{\text{net}}}{\dot{Q}_{\text{evap}}} \tag{33}$$

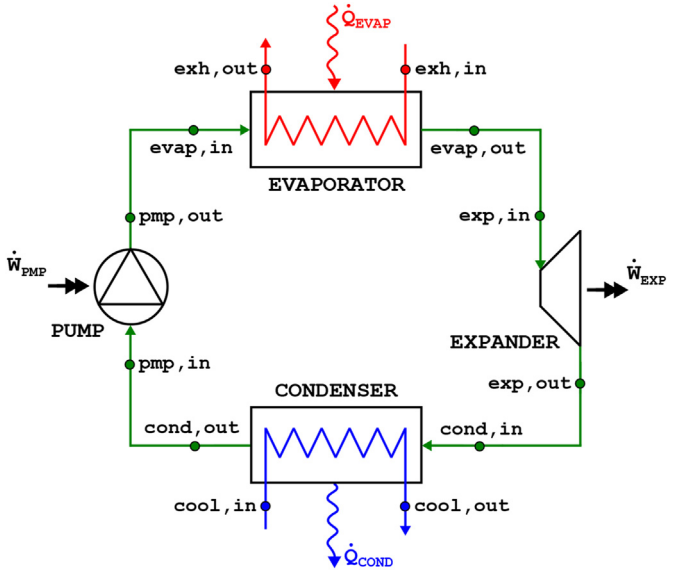

Fig. 16. Schematic of full cycle model.

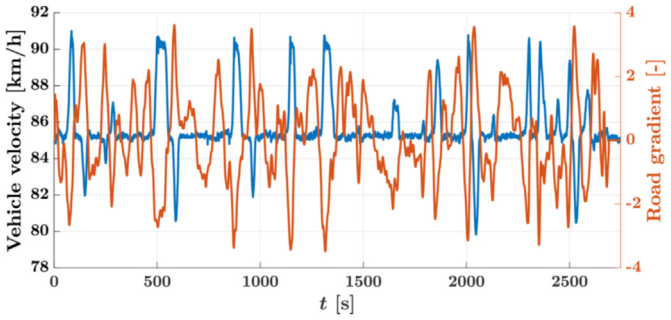

Fig. 17. Representative driving cycle for a long haul truck on an European road.

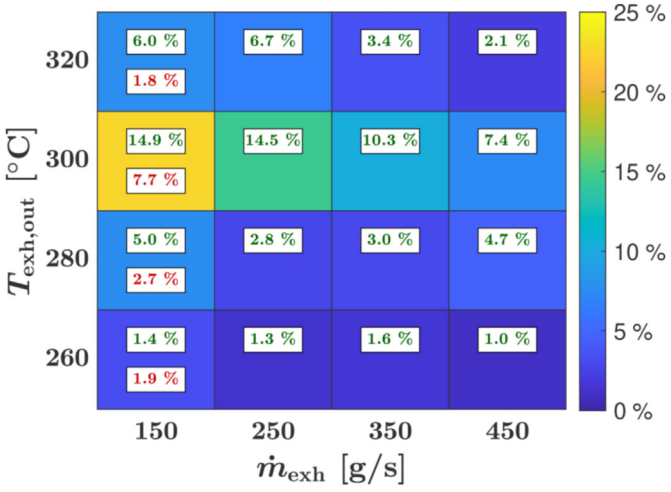

Fig. 18. Relative time distributions of the exhaust mass flow and temperature over the driving cycle. Green values indicate positive torque and red negative torque. The total drive cycle duration (Δt_{dc}) is 2748 s. (For interpretation of the references to colour in this figure legend, the reader is referred to the Web version of this article.)

The performance in the driving cycle is estimated using the definitions expressed in Eqs. (34) and (35). At positive engine torque (τ_{eng}), the expander power is directly provided to the engine, while at negative engine torque the expander power is converted into electrical power.

$$\dot{W}_{\text{pmp, el}} = \frac{\dot{W}_{\text{pmp}}}{\eta_{\text{el}}} \tag{34}$$

$$\dot{W}_{\text{exp}} = \begin{cases} \dot{W}_{\text{exp, mech}} = \eta_{\text{mech}} \dot{W}_{\text{exp}}, & \text{if } \tau_{\text{eng}} > 0 \\ \dot{W}_{\text{exp, el}} = \eta_{\text{el}} \dot{W}_{\text{exp}}, & \text{if } \tau_{\text{eng}} \leq 0 \end{cases} \tag{35}$$

5. Results and discussion

5.1. Steady-state performance

Steady-state simulations using the cycle model with water as the working fluid were performed for 16 engine operating points with exhaust mass flows ($\dot{m}_{\text{exh}}$) ranging from 150 to 450 g/s and exhaust outlet temperatures ($T_{\text{exh, out}}$) between 260 and 320 °C, as previously presented in Fig. 18 and Table 14. In the following discussion, these will be designated with an M for mass flow and a T for temperature. Thus, M150T300 corresponds to an exhaust mass flow of 150 g/s and an outlet temperature of 300 °C. The pump

Table 14
Cycle inputs and constraints.

Inputs			
Exhaust gas mass flow	$\dot{m}_{exh}$	150–450	g/s
Exhaust gas inlet temperature	$T_{exh,\ in}$	260–320	°C
Exhaust gas inlet pressure	$p_{exh,\ in}$	1.03–1.06	bar
Pump inlet subcooling temperature	ΔT_{sub}	5	K
Pump mechanical efficiency	η_{pmp}	0.50	–
Electrical generator efficiency	η_{el}	0.85	–
Mechanical coupling efficiency	η_{mech}	0.98	–
Constraints			
Pump outlet pressure	$p_{pmp,\ out}$	$10 - p_{crit}$	bar
Evaporator outlet temperature	$T_{evap,\ out}$	n/a – 260	°C
Evaporator outlet superheating temp.	ΔT_{sup}	10–30	K
Expander speed	N_{exp}	500–3500	rpm
Pump speed	N_{pmp}	150–6000	rpm

outlet pressures and mass flows at four engine operating points for a range of expander speeds are shown in Fig. 19. In these cases, the evaporator superheating temperature difference was kept within the constraints specified in Table 14. At each engine operating point, the exhaust temperature was kept constant while varying the mass flow, effectively changing the heat available for recovery.

As expected, the pump outlet pressure decreased as the expander speed increased and increased as the available exhaust heat increased (represented by the engine operating points). An increase in the available exhaust heat allows for higher cycle mass flows, as shown on the right of Fig. 19. The same effect was observed when increasing the expander speed. Increasing the expander speed (and thus reducing the evaporating pressure of water in the cycle, as explained further on; see Fig. 22) made it possible to recover more heat from the exhaust gases. The resulting net power, shown on the left of Fig. 20, depends on the required pump power, the amount of heat transferred from the heat source, and the expander power obtained. The pump power is determined by the pump efficiency, the pressure difference over the pump, and the mass flow. The amount of heat transferred from the source to the cycle is a function of the exhaust mass flow and temperature, as well as the cycle temperature, pressure, and mass flow. The expander power depends on how effectively the recovered heat is transformed into power, which is shown on the right of Fig. 20. Because of the interaction between the pump power, recovered heat, and expander power, there is no single optimal expander speed that maximizes the power output for all engine operating points. For the lower exhaust mass flows, the maximum net power is around 1.1 kW and is achieved at a relatively low expander speed of around 900 rpm. As the exhaust mass flow increases, both the power output and the optimal expander speed increase, with maxima of 4.2 kW and 2800 rpm, respectively.

Simulations were performed to obtain the maximum power output for the 16 engine operating points with water as the working fluid. The expander speed was varied at each operating point to obtain the maximum net power output, which is shown on the left of Fig. 21. The values shown at the edges of this figure were obtained by linear extrapolation. Depending on the exhaust mass flow and temperature, the recoverable net power ranges from 0 to 8 kW. Another important aspect for automotive applications is the amount of heat that must be rejected to allow condensation of the working fluid, which is shown on the right of Fig. 21. When using exhaust gases as a heat source, this heat must be either transferred to the coolant and rejected in the coolant radiator or rejected directly via a separate radiator. The results of the simulations show that the heat transfer rate in the condenser can be as high as 60 kW.

Simulations using the same cycle components were also performed with cyclopentane and ethanol as the working fluid, and the results all selected working fluids are shown in Table 15. The condensation pressure was set at 1.1 bar for all fluids, resulting in a different condensation temperature for each fluid. A lower condensation temperature means a smaller temperature difference between the working fluid and the ambient temperature, making it more difficult to reject excess heat. In a practical system, this could lead to increased power consumption by the cooling fan, which would reduce the net power output of the system. This effect is not taken into account here.

The results from Table 15 show that the highest power output was obtained with cyclopentane, then ethanol, and finally water. These differences in the performance can be explained by considering the M150T300 engine operating point, for which the results are shown in Table 16.

The power outputs for cyclopentane and ethanol were higher than for water because of higher mass flows and expander

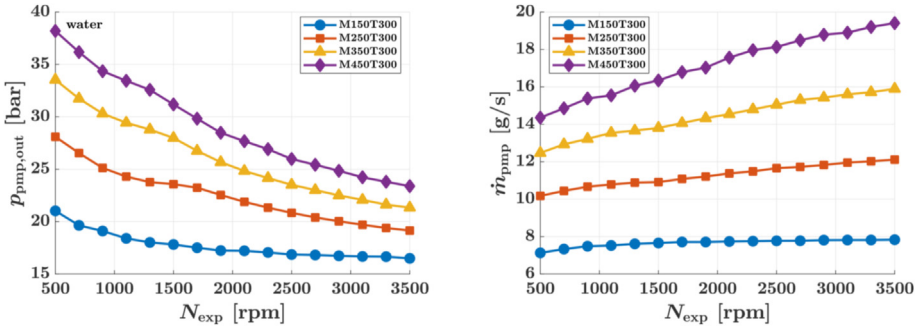

Fig. 19. Pump outlet pressure (left) and mass flow rate (right) for water as functions of the expander speed at different engine operating points.

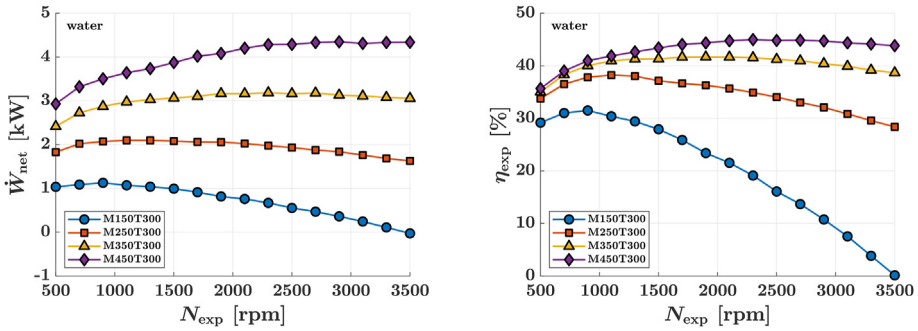

Fig. 20. Net shaft power (left) and expander efficiency (right) for water as functions of the expander speed at different engine operating points.

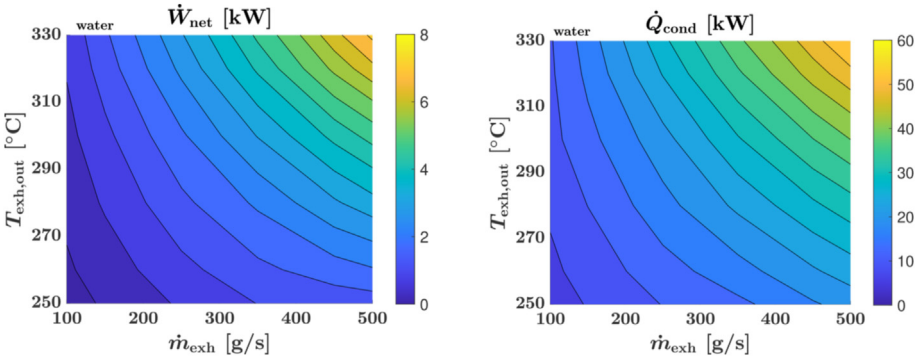

Fig. 21. Net shaft power (left) and condenser heat transfer rate (right) for water as a function of the exhaust mass flow and temperature. The values at the edges were linearly extrapolated.

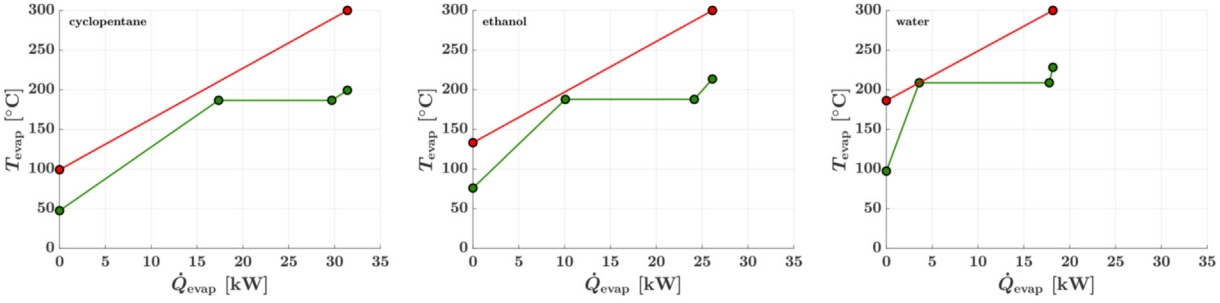

Fig. 22. QT-diagrams of cyclopentane, ethanol, and water for the M150T300 engine operating point.

Table 15
Range of cycle conditions for the 16 engine operating points.

Fluid	$\dot{m}_{pmp}$	p_{evap}	$T_{exp,\ in}$	N_{exp}	p_{cond}	T_{cond}	$\dot{Q}_{cond}$	$\dot{W}_{net}$	η_{th}
-	g/s	bar	°C	rpm	bar	°C	kW	kW	%
Cyclopent.	38.6–142	19.4–30.9	194–225	1285–3500	1.1	52	17.4–75.0	1.8–9.6	7.7–11
Ethanol	18.6–74.4	20.9–30.1	193–232	861–2774	1.1	80	14.6–66.3	1.0–7.8	5.9–9.8
Water	5.16–22.6	15.1–26.5	210–255	700–3139	1.1	102	10.2–45.8	0.5–5.7	3.7–10

efficiencies. The higher mass flows of cyclopentane and ethanol are due to the lower latent heat of these fluids and to a better thermal match between the heat source and the cycle. This is visualized in the heat transfer-temperature (QT) diagrams for the different working fluids at the M150T300 engine operating point, which are presented in Fig. 22. For cyclopentane, the temperature slope during preheating matches the temperature profile of the heat source, meaning that the heat transfer is not limited by the evaporating temperature of the working fluid and the maximum heat can be extracted for this specific heat exchanger geometry. For ethanol and especially for water, less heat can be extracted and a lower power output is achieved.

The corresponding temperature-entropy (Ts) diagrams are shown in Fig. 23. This shows that the expansion ends in the two-phase region in the cases of ethanol and water whereas for cyclopentane it ends in the superheated region. For most expanders,

Table 16
Cycle conditions for the M150T300 engine operating point.

Fluid	$\dot{m}_{pmp}$	p_{evap}	$T_{exp,\ in}$	N_{exp}	p_{cond}	T_{cond}	$\dot{Q}_{cond}$	$\dot{W}_{net}$	η_{th}
-	g/s	bar	°C	rpm	bar	°C	kW	kW	%
Cyclopentane	52.9	21.6	199	1546	1.1	52	27.7	2.75	8.7
Ethanol	25.2	23.4	214	1023	1.1	80	20.9	1.81	6.9
Water	7.45	18.7	228	1023	1.1	102	14.7	1.09	6.0

operation in the superheated region is preferable because it prevents droplets from damaging the expander. Additionally, when using cyclopentane, a recuperator could be added to improve the power output or reduce the condenser load. Although the Ts-diagrams suggest that the expander is operating at isentropic efficiency, this is not the case. During the expansion, not all of the available energy is converted to power; a significant portion is lost as heat, which is why two definitions for the expander power and energy change are necessary, as defined in Eq. (28) and Eq. (29).

5.2. Driving cycle performance

The exhaust flow and temperature over the driving cycle presented in Fig. 17 were used as inputs for the steady-state simulations of the three selected working fluids. The resulting net power outputs over the driving cycle of these fluids are shown in Fig. 24.

In accordance with the steady-state simulations, the best performance was obtained with cyclopentane, followed by ethanol and then water. To estimate performance over the whole driving cycle, the results were numerically integrated using a timestep (Δt) of 1 s:

$$W = \sum_{i=1}^{n} \dot{W}_i \Delta t \tag{36}$$

The integrated results for Eqs. (31), (34) and (35) are shown in Table 17, both in absolute and relative terms. The relative performance is obtained by dividing the absolute result by the total work done by the engine during the driving cycle (W_{dc} = 333 MJ). The results show that the WHR system can recover a significant amount of energy, corresponding to as much as 3.37% of the total engine energy requirement. This relative recovery can be roughly translated into fuel consumption reduction, assuming that the increased backpressure due to the exhaust evaporator does not affect the engine efficiency. The results also show that the recovered electrical work is comparable to the electrical work done by the pump, although it must be noted that the efficiencies of storing and extracting power from the battery are not included. Additionally, the table shows that the pump work is much higher for cyclopentane than for the other fluids because of the higher mass flow in the cycle. However, this is more than offset by the increase in expander power.

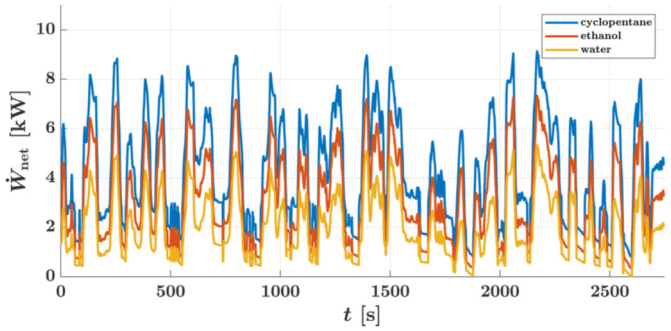

Fig. 24. Net shaft power for multiple fluids during the driving cycle.

Table 17
Driving cycle performance with a total engine work requirement of 333 MJ.

Fluid	Q_{cond}	$W_{pmp,\ el}$	$W_{exp,\ mech}$	$W_{exp,\ el}$	W^*_{net}
	MJ	MJ (%)	MJ (%)	MJ (%)	MJ (%)
Cyclopentane	100	1.62 (0.49)	11.7 (3.50)	1.17 (0.35)	11.2 (3.37)
Ethanol	86.1	0.90 (0.27)	8.42 (2.53)	0.69 (0.21)	8.21 (2.46)
Water	57.1	0.20 (0.06)	5.02 (1.51)	0.37 (0.11)	5.19 (1.56)

*$W_{net} = W_{exp,\ mech} + W_{exp,\ el} - W_{pmp,\ el}$.

Even though a driving cycle was used to evaluate the performance of the working fluids over the operational range of the engine during actual driving conditions, transient effects were ignored in this paper. The cycle components are assumed to react instantaneously to changes in the exhaust flow and temperature. In reality, the performance of the components will be affected by inertia during transient operation, with the thermal inertia in the heat exchangers being dominant [64]. This has important implications for the control of the system, as superheated conditions at the inlet of the expander should be ensured [14]. Another study [65] showed in a comparison between a steady state and transient model that a transient model will lead to lower fuel savings, although the resulting ranking remains the same. The expander coupling is another point of discussion. If the expander is mechanically coupled to the engine, its speed will be determined by

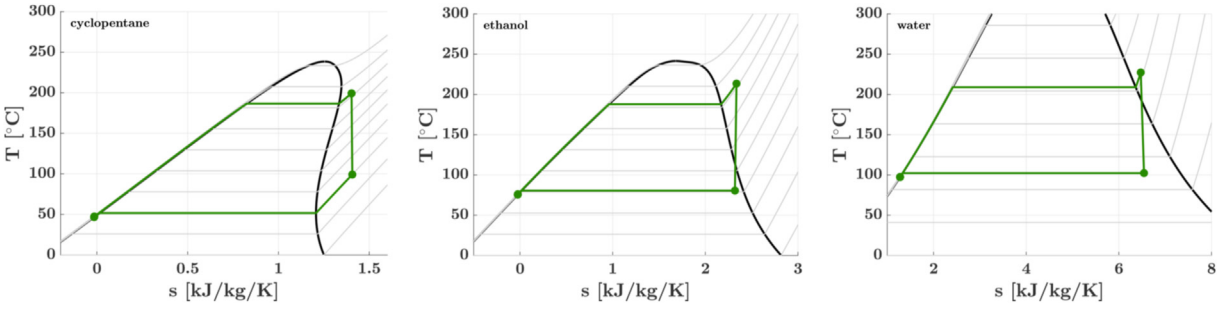

Fig. 23. Ts-diagrams of cyclopentane, ethanol, and water at the M150T300 engine operating point.

the engine speed and a predetermined gear ratio. However, the driving cycle results presented here were obtained under the assumption that the expander could operate at its optimal speed for which the corresponding power output were determined in the earlier steady-state simulations. The results in this section allow for comparison of different working fluids on the basis of their thermodynamic performance. In practice, however, the selection of the best working fluid is also subject to other constraints such as costs, component sizing, and environmental impact.

6. Conclusions

Experimental investigations were performed to evaluate the performance of a Rankine system with water for WHR from the exhaust gases of a heavy-duty engine. The results of these experiments constitute one of the main contributions of this paper. Additionally, models of the relevant cycle components were developed and then calibrated and validated against the experimental data. These models provided more detailed overview of the physical processes occurring within each component. This allowed for predictions of the performance of these components under conditions outside the experimental range and when using different working fluids. The component models were combined to create model of the full cycle, allowing the performance of the Rankine system to be simulated over a typical long haul truck driving cycle. The main results and conclusions obtained during this work were:

- Experimental results were obtained for a wide range of engine operating conditions. The experiments were divided into six distinct experimental sets and their results were used to calibrate and validate models of the main components of the Rankine cycle, i.e. the pump, pump bypass valve, evaporator, expander, and condenser. Experimental measurements of the expander shaft power were performed at four different engine operating points (A25, HW, A50, B25). The expander power ranged from 0.2 to 3 kW, corresponding to 0.2−2.5% of the engine power.
- Steady-state simulations of the Rankine cycle with water as the working fluid exhibited good agreement with the experimentally determined mass flow and evaporator heat transfer, but the expander power was overpredicted at low expander powers and underpredicted at high powers. Simulations performed at 16 engine operating points gave net power outputs between 0.5 and 5.7 kW, and the optimal expander speed was found to be dependent on the engine operating point. The added heat needing to be rejected in the condenser was between 10 and 46 kW. These values can be extrapolated to obtain results for the full range of operating conditions, yielding net power outputs between 0 and 8 kW and condenser heat transfer rates between 0 and 60 kW.
- To evaluate the performance of different working fluids in the studied WHR system, simulations were also performed with cyclopentane and ethanol as the working fluids. The results indicated that the evaporating pressures and expander inlet temperatures for these fluids were similar to those of water, but that they had higher mass flows in the cycle. The increased mass flows were a result of the lower latent heat and a better thermal match with the heat source, allowing for more heat transfer between source and cycle. Because of the higher flows and expander efficiencies, cyclopentane and ethanol outperformed water, providing net power outputs between 1.8 and 9.6 kW and 1.0 and 7.8 kW, respectively.
- The steady-state results for the three working fluids were used to simulate the performance over a typical driving cycle of a long haul truck. Although transient effects were not taken into account and the expander speed was not controlled by the engine speed (as would be the case in a real system due to the mechanical coupling), the results still allow for a comparison between the thermodynamic performance of the systems with the different working fluids. The total recovered energy during the driving cycle was 11.2, 8.2, and 5.2 MJ for cyclopentane, ethanol, and water, respectively, corresponding to recoveries of 3.4, 2.5, and 1.6% relative to the total energy requirement of the engine.

Declaration of competing interest

The authors declare that they have no known competing financial interests or personal relationships that could have appeared to influence the work reported in this paper.

Acknowledgments

This research was made possible by funding provided by the Strategic Vehicle Research and Innovation Programme (FFI) of the Swedish Energy Agency. The authors would like to thank the partners in the WHR project: Gnutti Carlo, IAV, Lund University, Scania, TitanX, Volvo Cars, and Volvo Group.

Nomenclature

A	area (m^2)
C_d	discharge coefficient (−)
h	specific enthalpy (J/kg)
MW	molecular weight (kg/kmol)
$\dot{m}$	mass flow rate (kg/s)
N	rotational speed (rpm)
p	pressure (Pa)
$\dot{Q}$	heat transfer rate (W)
s	entropy (J/kg/K)
t	time (s)
T	temperature (K)
V	volume (m^3)
$\dot{V}$	volume flow rate (m^3/s)
$\dot{W}$	power (W)

Greek symbols

η	efficiency (−)
ε	effectiveness (−)
φ_f	filling factor (−)
ρ	density (kg/m^3)
τ	torque (Nm)

Subscripts

amb	ambient
bpv	bypass valve
cond	condenser
cool	coolant
corr	correction
crit	critical

Subscripts (continued)

el	electrical
eng	engine
evap	evaporator
exh	exhaust

exp	expander
is	isentropic
mech	mechanical
pmp	pump
sh	shaft
sub	subcooled
sup	superheated
th	theoretical/thermodynamic

Abbreviations

CAC	charge air cooler
BPV	bypass valve
EGR	exhaust gas recirculation
EGRC	exhaust gas recirculation cooler
ESC	European stationary cycle
HD	heavy-duty
HDD	heavy-duty Diesel
HW	highway
GHG	greenhouse gas
GWP	global warming potential
ODP	ozone depletion potential
ORC	organic Rankine cycle
SV	safety valve
WHR	waste heat recovery

References

[1] International Energy Agency. Energy technology Perspectives 2020. 2020.
[2] European Environment Agency (EEA). National emissions reported to the UNFCCC and to the EU greenhouse gas monitoring mechanism. 2017. https://www.eea.europa.eu/ds_resolveuid/a6e1bc85fbed4989b0fd6739c443739a. [Accessed 15 December 2020].
[3] European Parliament, Council of the European Union. Regulation (EU) 2019/1242 - Setting CO2 emission performance standards for new heavy-duty vehicles. 2019.
[4] Hofer F, Gruber W, Raser B, Theißl H. Technology scenarios for fulfilling future EU CO2 targets for commercial vehicle fleets. ATZheavy duty worldwide 2020;13(1).
[5] Pischinger S, Schaub J, Aubeck F, van der Put D. Powertrain concepts for heavy-duty applications to meet 2030 CO2 regulations. ATZheavy duty worldwide 2020;13(3).
[6] Rijpkema J, Munch K, Andersson SB. Thermodynamic potential of twelve working fluids in Rankine and flash cycles for waste heat recovery in heavy duty diesel engines. Energy 2018;160.
[7] Aghaali H, Ångström H-E. A review of turbocompounding as a waste heat recovery system for internal combustion engines. Renew Sustain Energy Rev 2015;49.
[8] W. Bou Nader, J. Chamoun, and C. Dumand, "Thermoacoustic engine as waste heat recovery system on extended range hybrid electric vehicles," Energy Convers Manag, vol. 215, 2020.
[9] Lan S, Smith A, Stobart R, Chen R. Feasibility study on a vehicular thermoelectric generator for both waste heat recovery and engine oil warm-up. Appl Energy 2019;242.
[10] Di Battista D, Fatigati F, Carapellucci R, Cipollone R. Inverted Brayton Cycle for waste heat recovery in reciprocating internal combustion engines. Appl Energy 2019;253.
[11] Güven M, Bedir H, Anlas G. Optimization and application of Stirling engine for waste heat recovery from a heavy-duty truck engine. Energy Convers Manag 2019;180.
[12] Trabucchi S, De Servi C, Casella F, Colonna P. Design, modelling, and control of a waste heat recovery unit for heavy-duty truck engines. Energy Procedia 2017;129.
[13] Xu B, Rathod D, Yebi A, Filipi Z, Onori S, Hoffman M. A comprehensive review of organic rankine cycle waste heat recovery systems in heavy-duty diesel engine applications. Renew Sustain Energy Rev 2019;107.
[14] Feru E, Willems F, de Jager B, Steinbuch M. Modeling and control of a parallel waste heat recovery system for euro-VI heavy-duty diesel engines. Energies 2014;7(10).
[15] Mahmoudi A, Fazli M, Morad MR. A recent review of waste heat recovery by Organic Rankine Cycle. Appl Therm Eng 2018;143.
[16] Rijpkema J, Andersson S, Munch K. Thermodynamic cycle and working fluid selection for waste heat recovery in a heavy duty diesel engine. SAE Technical Paper 2018-01-1371 2018.
[17] Preißinger M, Schwöbel JA, Klamt A, Brüggemann D. Multi-criteria evaluation of several million working fluids for waste heat recovery by means of Organic Rankine Cycle in passenger cars and heavy-duty trucks. Applied Energy; 2017.
[18] Schilling J, Eichler K, Kölsch B, Pischinger S, Bardow A. Integrated design of working fluid and organic Rankine cycle utilizing transient exhaust gases of heavy-duty vehicles. Appl Energy 2019;255.
[19] Li X, Song J, Yu G, Liang Y, Tian H, Shu G, Markides CN. Organic Rankine cycle systems for engine waste-heat recovery: heat exchanger design in space-constrained applications. Energy Convers Manag 2019;199.
[20] B. Xu, D. Rathod, A. Yebi, S. Onori, Z. Filipi, and M. Hoffman, "A comparative analysis of dynamic evaporator models for organic Rankine cycle waste heat recovery systems," Appl Therm Eng, vol. 165, 2020.
[21] Alshammari F, Karvountzis-Kontakiotis A, Pesyridis A, Usman M. Expander technologies for automotive engine organic rankine cycle applications. Energies 2018;11.
[22] Guillaume L, Lemort V. Comparison of different ORC typologies for heavy-duty trucks by means of a thermo-economic optimization. Energy 2019;182.
[23] Imran M, Haglind F, Lemort V, Meroni A. Optimization of organic rankine cycle power systems for waste heat recovery on heavy-duty vehicles considering the performance, cost, mass and volume of the system. Energy 2019;180.
[24] Galuppo F, Nadri M, Dufour P, Reiche T, Lemort V. Evaluation of a coupled organic rankine cycle mild hybrid architecture for long-haul heavy-duty truck. IFAC-PapersOnLine 2019;52.
[25] Huster WR, Vaupel Y, Mhamdi A, Mitsos A. Validated dynamic model of an organic Rankine cycle (ORC) for waste heat recovery in a diesel truck. Energy 2018;151.
[26] Koppauer H, Kemmetmüller W, Kugi A. Modeling and optimal steady-state operating points of an ORC waste heat recovery system for diesel engines. Appl Energy 2017;206.
[27] Xu B, Rathod D, Kulkarni S, Yebi A, Filipi Z, Onori S, Hoffman M. Transient dynamic modeling and validation of an organic Rankine cycle waste heat recovery system for heavy duty diesel engine applications. Appl Energy 2017;205.
[28] Neunteufl K, Stevenson PM, Hülser H, Theissl H. Better fuel consumption by waste heat recovery. MTZ worldwide 2012;73(12).
[29] Freymann R, Strobl W, Obieglo A. The turbosteamer: a system introducing the principle of cogeneration in automotive applications. MTZ worldwide 2008;69(5).
[30] Freymann R, Ringler J, Seifert M, Horst T. The second generation turbosteamer. MTZ worldwide feb 2012;73.
[31] Seher D, Lengenfelder T, Gerhardt J, Eisenmenger N, Hackner M, Krinn I. "Waste heat recovery for commercial vehicles with a rankine process," 21 st Aachen Colloquium Automobile and engine technology. 2012.
[32] Koeberlein D. Cummins SuperTruck Program. Technology and system Level Demonstration of highly efficient and Clean, Diesel powered Class 8 trucks. Department of Energy Annual Merit Review; 2014.
[33] Dickson J, Damon K. Cummins/peterbilt Supertruck II. Department of Energy Annual Merit Review; 2019.
[34] Allain M, Atherton D, Gruden I, Singh S, Sisken K. Daimler's super truck program; 50 % brake thermal efficiency. In: 2012 Directions in engine-efficiency and emissions research (DEER) Conference; 2012.
[35] Endo T, Kawajiri S, Kojima Y, Takahashi K, Baba T, Ibaraki S, Takahashi T, Shinohara M. Study on maximizing exergy in automotive engines. SAE Trans: Journal of Engines 2007;116.
[36] Marlok H, Bucher M, Ferrand N. Further Development of exhaust waste heat recovery, vol. 13. ATZheavy duty worldwide; 2020. 3.
[37] Thantla S, Fridh J, Erlandsson A, Aspfors J. Performance Analysis of volumetric expanders in heavy-duty truck waste heat recovery. SAE Technical Paper 2019-01-2266; 2019.
[38] Carstensen A, Horn A, Klammer J, Gockel J. Waste heat recovery in Passenger Cars and trucks, vol. 80. MTZ worldwide; 2019. 4.
[39] Ekström F. A mild hybrid SIDI turbo passenger car engine with Rankine waste heat recovery. SAE Technical Paper 2019-24-0194; 2019.
[40] Rijpkema J, Ekström F, Munch K, Andersson SB. Experimental results of a waste heat recovery system with ethanol using the exhaust gases of a light-duty engine. In: Proceedings of the 5th International Seminar on ORC power systems; 2019.
[41] Bettoja F, Perosino A, Lemort V, Guillaume L, Reiche T, Wagner T. NoWaste: waste heat Re-use for greener truck. Transportation Research Procedia 2016;14.
[42] Furukawa T, Nakamura M, Machida K, Shimokawa K. A study of the rankine cycle generating system for heavy duty HV trucks. apr 2014.
[43] Yang K, Zhang H, Song S, Zhang J, Wu Y, Zhang Y, Wang H, Chang Y, Bei C. Performance analysis of the vehicle diesel engine-ORC combined system based on a screw expander. Energies 2014;7.
[44] Zhang Y-Q, Wu Y-T, Xia G-D, Ma C-F, Ji W-N, Liu S-W, Yang K, Yang F-B. Development and experimental study on organic Rankine cycle system with single-screw expander for waste heat recovery from exhaust of diesel engine. Energy 2014;77.
[45] Latz G, Erlandsson O, Skåre T, Contet A, Andersson S, Munch K. Performance analysis of a reciprocating piston expander and a plate type exhaust gas recirculation boiler in a water-based Rankine cycle for heat recovery from a heavy duty diesel engine. Energies 2016;9(7).
[46] Shu G, Yu G, Tian H, Wei H, Liang X, Huang Z. "Multi-approach evaluations of a cascade-Organic Rankine Cycle (C-ORC) system driven by diesel engine waste heat: Part A – thermodynamic evaluations. Energy Convers Manag 2016;108.
[47] Yu G, Shu G, Tian H, Huo Y, Zhu W. Experimental investigations on a cascaded steam-/organic-Rankine-cycle (RC/ORC) system for waste heat recovery

(WHR) from diesel engine. Energy Convers Manag 2016;129.
[48] Shi L, Shu G, Tian H, Huang G, Chen T, Li X, Li D. Experimental comparison between four CO 2 -based transcritical Rankine cycle (CTRC) systems for engine waste heat recovery. Energy Convers Manag 2017;150.
[49] Guillaume L, Legros A, Desideri A, Lemort V. Performance of a radial-inflow turbine integrated in an ORC system and designed for a WHR on truck application: an experimental comparison between R245fa and R1233zd. Appl Energy 2017;186.
[50] Alshammari F, Pesyridis A, Karvountzis-Kontakiotis A, Franchetti B, Pesmazoglou Y. Experimental study of a small scale organic Rankine cycle waste heat recovery system for a heavy duty diesel engine with focus on the radial inflow turbine expander performance. Appl Energy 2018;215.
[51] Alshammari F, Pesyridis A. Experimental study of organic Rankine cycle system and expander performance for heavy-duty diesel engine. Energy Convers Manag 2019;199.
[52] Shu G, Zhao M, Tian H, Huo Y, Zhu W. Experimental comparison of R123 and R245fa as working fluids for waste heat recovery from heavy-duty diesel engine. Energy 2016;115.
[53] Taylor J. An introduction to error Analysis: the study of Uncertainties in physical measurements. University Science Books; 1997.
[54] "DieselNet: Emission test cycles - European Stationary Cycle (ESC)." https://www.dieselnet.com/standards/cycles/esc.php. Accessed: 2020-07-02.
[55] Danfoss. Nessie high pressure pumps for technical water, type PAH. Data Sheet; 2007.
[56] Webb R, Nae-Hyun K. Principles of Enhanced heat transfer. CRC Press; 2005.
[57] Lemort V. Contribution to the Characterization of Scroll Machines in Compressor and expander Modes. PhD thesis; 2008.
[58] Rijpkema J, Andersson S, Munch K, Thantla S, Fridh J. Experimental investigation and modeling of a reciprocating piston expander for waste heat recovery from a truck engine. " Applied Thermal Engineering; 2020.
[59] MathWorks. MATLAB, Version R2019a. 2019.
[60] Bell IH, Wronski J, Quoilin S, Lemort V. Pure and pseudo-pure fluid thermophysical property evaluation and the open-source thermophysical property library CoolProp. Ind Eng Chem Res 2014;53(6).
[61] Galuppo F, Reiche T, Lemort V, Dufour P, Nadri M. Organic Rankine Cycle based waste heat recovery modeling and control of the low pressure side using direct condensation and dedicated fans. Energy; 2020.
[62] Rijpkema J, Munch K, Andersson SB. Combining low- and high-temperature heat sources in a heavy duty diesel engine for maximum waste heat recovery using rankine and flash cycles. In: Junior C, Dingel O, editors. ". Energy and thermal management, air-Conditioning, and waste heat Utilization. Springer International Publishing; 2019.
[63] Bredel E, Nickl J, Bartosch S. Waste heat recovery in drive systems of Today and Tomorrow, vol. 72. MTZ worldwide; 2011.
[64] S. Quoilin, R. Aumann, A. Grill, A. Schuster, V. Lemort, and H. Spliethoff, "Dynamic modeling and optimal control strategy of waste heat recovery Organic Rankine Cycles," Appl Energy, vol. 88, 2011.
[65] Grelet V, Reiche T, Lemort V, Nadri M, Dufour P. Transient performance evaluation of waste heat recovery rankine cycle based system for heavy duty trucks. Appl Energy 2016;165.